

# Circulation Factors Determining the Propagation Speed of the Madden–Julian Oscillation

GUOSEN CHEN

*Earth System Modeling Center, Key Laboratory of Meteorological Disaster of Ministry of Education, Collaborative Innovation Center on Forecast and Evaluation of Meteorological Disasters, Nanjing University of Information Science and Technology, Nanjing, China, and Department of Atmospheric Sciences and International Pacific Research Center, University of Hawai'i at Mānoa, Honolulu, Hawaii*

BIN WANG

*Department of Atmospheric Sciences and International Pacific Research Center, University of Hawai'i at Mānoa, Honolulu, Hawaii, and Earth System Modeling Center, Key Laboratory of Meteorological Disaster of Ministry of Education, Collaborative Innovation Center on Forecast and Evaluation of Meteorological Disasters, Nanjing University of Information Science and Technology, Nanjing, China*

(Manuscript received 5 September 2019, in final form 22 January 2020)


## ABSTRACT

The eastward propagating Madden–Julian oscillation (MJO) events exhibit various speeds ranging from 1 to 9 m s<sup>-1</sup>, but what controls the propagation speed remains elusive. This study attempts to address this issue. It reveals that the Kelvin wave response (KWR) induced by the MJO convection is a major circulation factor controlling the observed propagation speed of the MJO, with a stronger KWR corresponding to faster eastward propagation. A stronger KWR can accelerate the MJO eastward propagation by enhancing the low-level premoistening and preconditioning to the east of the MJO deep convection. The strength of the KWR is affected by the background sea surface temperature (SST). When the equatorial central Pacific SST warms, the zonal scale of the Indo-Pacific warm pool expands, which increases the zonal scale of the MJO, favoring enhancing the KWR. This effect of warm-pool zonal scale has been verified by idealized experiments using a theoretical model. The findings here shed light on the propagation mechanism of the MJO and provide a set of potential predictors for forecasting the MJO propagation.

## 1. Introduction

The slow eastward propagation of convective anomalies over the Indo-Pacific warm pool region is the most fundamental feature of the Madden–Julian oscillation (MJO) (Madden and Julian 1972). Explanation of this slow eastward propagation is a central issue in studies of the MJO. The observed MJO eastward propagation speed exhibits a broad range from about 2 to 9 m s<sup>-1</sup> (Knutson et al. 1986; Zhang and Ling 2017). Understanding what accelerates or retards the MJO propagation can provide physical insight into the nature of MJO propagation.

Recent studies have shown that there exist propagating and nonpropagating MJOs in both observations (Kim et al. 2014; Feng et al. 2015; Chen and Wang 2018) and GCMs (Jiang et al. 2015; Jiang 2017; Wang and Lee 2017). The propagating MJO is a type of MJO that can propagate from the Indian Ocean (IO) to the western Pacific (WP), while the nonpropagating MJO is a type of MJO that originates from the IO but cannot propagate across the Maritime Continent (MC). It is shown that zonal structural asymmetry distinguishes the propagating and nonpropagating MJOs. Matthews (2000) argued that the dry anomalies leading the MJO major convection can excite Rossby wave anticyclonic gyres, facilitating the eastward propagation of MJO by inducing surface convergence. Kim et al. (2014) showed that the existence of the leading dry anomalies distinguishes the propagating and nonpropagating MJOs. Chen and Wang (2018) showed that the leading dry anomalies

 Denotes content that is immediately available upon publication as open access.

Corresponding author: Guosen Chen, guosen@nuist.edu.cn

DOI: 10.1175/JCLI-D-19-0661.1

© 2020 American Meteorological Society. For information regarding reuse of this content and general copyright information, consult the AMS Copyright Policy ([www.ametsoc.org/PUBSRreuseLicenses](http://www.ametsoc.org/PUBSRreuseLicenses)).

enhance the front Walker cell and the Kelvin wave response (KWR) to the east of the MJO major convection, facilitating the MJO eastward propagation by enhancing the boundary layer (BL) moisture convergence. The zonal structural asymmetries in the vertical structures of the moisture, vertical velocity, and diabatic heating are also characteristics of the eastward propagation of the MJO (Jiang et al. 2015; Wang and Lee 2017; Wang et al. 2018). Wang and Lee (2017) attributed these zonal asymmetries in vertical structures to the asymmetry between the KWR and Rossby wave response to the MJO convection.

Recent studies have also revealed that there exist slow and fast propagating MJO in both observations and GCMs. Yadav and Straus (2017) showed that there exist slow and fast propagating MJO episodes in observations, but they focused on the tropical–extratropical interaction associated with the slow and fast MJO episodes. By examining 24 GCM outputs, Jiang et al. (2015) showed that the MJO in some GCMs tended to propagate more slowly than the observed average MJO speed (their Fig. 4), but they focused on comparing the propagating and nonpropagating MJO. In a pilot study of MJO diversity, Wang et al. (2019) have shown that observed MJO events can be classified into four clusters: standing, jumping, slow eastward propagation, and fast eastward propagation. Each type exhibits distinctive east–west asymmetric circulation and thermodynamic structures. Tight coupling between the KWR and MJO major convection is unique for the propagating (slow and fast) events, as opposed to the nonpropagating (standing and jumping) events, while the strength and length of KWR distinguish slow and fast propagating clusters. However, their study focused on the causes of the diversified MJO propagation patterns and did not fully address what controls the propagation speed of the MJO.

This study aims to identify factors controlling the MJO propagation speed in observations. Built upon the previous findings, we speculate that the MJO propagation speed is linked to its structural characteristics. Moreover, as the MJO structure is controlled and modified by the background mean moisture (or moist static energy) state (Wang and Xie 1997; Wang and Chen 2017; Jiang et al. 2018), it is also interesting to ask how the background mean states modify the MJO propagation speed through affecting the MJO structures.

## 2. Data and methods

### a. Data

The atmospheric data used in this study are the four times daily,  $2.5^\circ$  longitude  $\times$   $2.5^\circ$  latitude horizontal resolution ERA-Interim reanalysis dataset (Dee et al.

2011), with period from 1979 through 2013. The daily mean is calculated from the four times daily records, and 19 vertical levels from 1000 to 100 hPa with 50-hPa intervals are selected. The wind components, geopotential height, temperature, and specific humidity were used. Daily averages of outgoing longwave radiation (OLR) data on a  $2.5^\circ$  square grid, sourced from the NOAA/NCEP interpolated OLR dataset, were used as a proxy for large-scale convection over the tropical region (Liebmann and Smith 1996). As the organized eastward propagation of the MJO is most prominent and regular during the boreal winter (Kikuchi et al. 2012), we focus on the MJO events in the boreal winter from November to April (NDJFMA). To study the background sea surface temperature (SST) conditions, the SST dataset from the NOAA Extended Reconstructed Sea Surface Temperature (ERSST) version 5 (Huang et al. 2017) has been adopted. To obtain the intraseasonal signals, the data filtering process following Chen and Wang (2018) has been applied to the daily data. First, the time-mean and first three harmonics of climatological seasonal cycle are removed from the daily field. Then a 20–70-day Lanczos bandpass filter (Duchon 1979) is applied to the data.

### b. Methods for obtaining wave components

The normal-mode function expansion method derived by Kasahara (1976) and Kasahara and Puri (1981) was used to distill the wave responses induced by the MJO convection. The essence of this method is to project atmospheric data onto a set of Hough functions, which are solutions of Laplace's tidal equations on a sphere (Longuet-Higgins 1968). The Hough functions contain eastward gravity wave modes, westward gravity wave modes, and rotational wave modes (Kasahara 1976), making it suitable for decomposing atmospheric data into certain wave components (Žagar and Franzke 2015), such as Kelvin waves (the first mode in the eastward gravity wave modes) and Rossby waves (the rotational modes). The details of this method are given in appendix A.

### c. Selecting MJO events and tracking MJO propagation speed

The method for selecting MJO events is similar to that in the previous studies (Chen and Wang 2018; Wang et al. 2019). An MJO event is selected if the area averaged OLR anomaly over the eastern equatorial IO ( $80^\circ$ – $100^\circ$ E,  $10^\circ$ S– $10^\circ$ N) is below its mean by one standard deviation. If there are consecutive days meeting this criterion, it is treated as one event. We define the day with the lowest OLR index as day 0 of that event. There are 127 MJO events over the IO region during the boreal winter (NDJFMA) in the period of 1979–2013.

TABLE 1. Dates of day 0, starting day, and ending day for the selected 58 propagating MJO.

Slow			Intermediate			Fast		
Start	End	Day 0	Start	End	Day 0	Start	End	Day 0
4 Nov 1979	7 Dec 1979	20 Nov 1979	23 Nov 1981	19 Dec 1981	28 Nov 1981	5 Apr 1980	21 Apr 1980	10 Apr 1980
16 Dec 1982	13 Jan 1983	23 Dec 1982	19 Oct 1986	15 Nov 1986	1 Nov 1986	5 Jan 1982	18 Jan 1982	10 Jan 1982
16 Apr 1983	7 May 1983	21 Apr 1983	17 Jan 1988	29 Feb 1988	25 Jan 1988	13 Apr 1982	10 May 1982	22 Apr 1982
31 Oct 1983	23 Nov 1983	8 Nov 1983	26 Mar 1989	20 Apr 1989	8 Apr 1989	28 Jan 1985	12 Mar 1985	8 Feb 1985
26 Feb 1984	17 Mar 1984	1 Mar 1984	8 Apr 1991	7 May 1991	15 Apr 1991	2 Dec 1987	3 Jan 1988	7 Dec 1987
2 Apr 1985	25 Apr 1985	13 Apr 1985	19 Apr 1995	26 May 1995	30 Apr 1995	12 Mar 1988	9 Apr 1988	21 Mar 1988
29 Dec 1985	29 Jan 1986	7 Jan 1986	4 Feb 1997	12 Mar 1997	14 Feb 1997	7 Jan 1990	15 Feb 1990	16 Jan 1990
5 Nov 1988	22 Dec 1988	7 Nov 1988	24 Mar 1997	21 Apr 1997	2 Apr 1997	17 Feb 1990	21 Mar 1990	28 Feb 1990
5 Jan 1989	2 Feb 1989	17 Jan 1989	7 Jan 1999	2 Feb 1999	22 Jan 1999	15 Dec 1991	11 Jan 1992	26 Dec 1991
6 Nov 1994	4 Jan 1995	2 Dec 1994	19 Nov 1999	19 Dec 1999	6 Dec 1999	19 Mar 1992	26 Apr 1992	31 Mar 1992
21 Dec 1994	2 Feb 1995	7 Jan 1995	9 Nov 2000	3 Dec 2000	19 Nov 2000	5 Jan 1993	30 Jan 1993	18 Jan 1993
15 Nov 1996	29 Dec 1996	6 Dec 1996	18 Jan 2004	13 Feb 2004	28 Jan 2004	12 Jan 1994	28 Jan 1994	19 Jan 1994
20 Jan 2001	2 Feb 2001	1 Feb 2001	6 Jan 2006	9 Feb 2006	12 Jan 2006	24 Mar 1995	9 Apr 1995	27 Mar 1995
7 Nov 2001	29 Dec 2001	20 Nov 2001	15 Mar 2006	3 Apr 2006	20 Mar 2006	21 Apr 2002	21 May 2002	30 Apr 2002
11 Dec 2002	12 Jan 2003	24 Dec 2002	23 Dec 2009	12 Feb 2010	31 Dec 2009	4 Nov 2002	10 Dec 2002	14 Nov 2002
16 Feb 2006	11 Mar 2006	21 Feb 2006	19 Oct 2011	13 Nov 2011	1 Nov 2011	23 Apr 2004	11 May 2004	29 Apr 2004
3 Dec 2007	27 Jan 2008	12 Dec 2007	23 Feb 2012	1 Apr 2012	8 Mar 2012	22 Apr 2005	15 May 2005	30 Apr 2005
17 Jan 2008	18 Feb 2008	29 Jan 2008	26 Mar 2013	14 Apr 2013	1 Apr 2013	16 Dec 2006	9 Jan 2007	26 Dec 2006
27 Oct 2009	10 Dec 2009	12 Nov 2009				3 Apr 2009	29 Apr 2009	10 Apr 2009
5 Feb 2013	27 Feb 2013	7 Feb 2013				22 Dec 2012	9 Jan 2013	27 Dec 2012

The propagation trajectories in the time–longitude section of these MJO events are then tracked. The method for MJO tracking here is essentially the same as the one proposed by [Zhang and Ling \(2017\)](#), with some modifications. The essence of this method is to find a tracking line that best describes the eastward propagation of MJO convection anomalies in the time–longitude section. The differences between the modified method used here and the original method are described in [appendix B](#). The original method may overestimate the MJO propagation speed (see [Fig. B1](#) and the associated information in [appendix B](#)). This tracking method gives the following information: mean propagation speed, the starting and ending dates, and the starting and ending longitudes of individual MJO event.

#### d. Classification of MJO events

In this study, we are interested in those MJO events that initiate in the IO and propagate eastward for a certain distance. Thus, the MJO events are further selected if the tracking line faithfully represents the eastward propagation of convective anomalies, and the tracking line starts from west of 82.5°E and goes beyond 120°E. We define these events as propagating MJO events, and 58 propagating MJO events were identified. [Table 1](#) shows the starting and ending dates, as well as day 0, of these propagating MJO events.

[Figure 1a](#) shows that the 58 propagating MJO events exhibit various propagation speeds ranging from 1 to 9 m s<sup>-1</sup>. The speeds show a bimodal distribution, with one peak around 3–4 m s<sup>-1</sup> and the other around 5–6 m s<sup>-1</sup>,

suggesting that the 58 selected propagating MJO events can be roughly grouped into slow MJO group (<4 m s<sup>-1</sup>; 20 cases) and fast MJO group (>5.1 m s<sup>-1</sup>; 20 cases). [Figures 1b and 1c](#) show the composited Hovmöller diagrams for the slow and fast MJO groups. It reveals that the convection anomalies in the fast MJO propagate faster and farther east than those in the slow MJO.

### 3. Observational results

#### a. Circulation factors affecting the MJO propagation speed

What are the circulation factors distinguishing the slow and fast MJOs? [Figures 2a and 2b](#) show that as the convection anomalies mature in the IO, the anomalous circulation of the MJO develops into a coupled Kelvin–Rossby wave structure, reminiscent of the Gill–Matsuno pattern ([Matsuno 1966](#); [Gill 1980](#)), with KWR to the east of the MJO major convection and Rossby wave response to the west. There are two salient differences between the slow and fast MJO groups. One is that the fast MJO has stronger KWR. The other is that the fast MJO has larger zonal scales in convection and circulation.

To quantify the KWR, we use Hough function expansion to distill the KWR from the composited circulation anomalies. The results are shown in [Figs. 2c and 2d](#). It confirms that the KWR in the fast MJO is much stronger than that in the slow MJO according to the amplitude of geopotential anomaly filtered for the Kelvin wave mode, suggesting that the strength of the

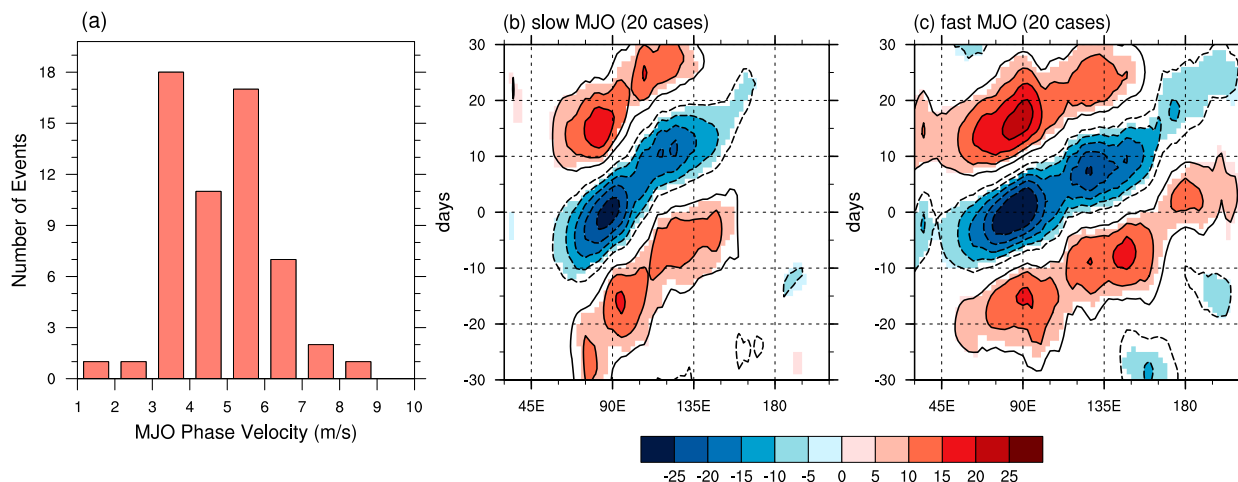


FIG. 1. Distribution of MJO propagation speed and propagation features of slow and fast MJO events. (a) The histogram of propagation speed for the 58 propagating MJO events. The composited Hovmöller diagrams of the equatorial ( $10^{\circ}\text{S}$ – $10^{\circ}\text{N}$  averaged) OLR ( $\text{W m}^{-2}$ ) are shown for the (b) slow and (c) fast MJO events. The contour interval is  $5 \text{ W m}^{-2}$ . The OLR anomalies above 95% confidence level are shaded.

KWR could be a factor controlling the propagation speed of the MJO. To further quantify the relationships between the KWR and MJO propagation speed, we defined a Kelvin wave index for the 58 selected propagating MJO. Since the MJO is a planetary-scale phenomenon (Madden and Julian 1972; Zhang 2005) and the associated Kelvin wave response is located to the east of the MJO major convection [i.e. a Gill-like pattern, (Gill 1980)], the Kelvin wave index is defined as

$$\text{Kelvin wave index} = \frac{1}{90^{\circ}} \int_{\text{lon}_c}^{\text{lon}_c + 90^{\circ}} Z_K d\text{lon}, \quad (1)$$

where  $Z_K$  is the pentad mean (from day  $-2$  to day  $2$ ) 850-hPa geopotential height anomaly of the KWR along the equator;  $\text{lon}_c$  is the longitude of the minimum equatorial ( $15^{\circ}\text{S}$ – $15^{\circ}\text{N}$ ) OLR. For comparison, the circulation has been scaled to a minimum equatorial ( $15^{\circ}\text{S}$ – $15^{\circ}\text{N}$ ) OLR of  $-30 \text{ W m}^{-2}$  before calculating the Kelvin wave index. The Kelvin wave index measures the mean strength of the KWR to the peak phase of MJO convection in IO (defined as the pentad centered on day 0, i.e., day  $-2$  to day  $2$ ).

Figure 3a shows that the Kelvin wave index is significantly correlated with the MJO propagation speed with a linear correlation coefficient of 0.64 (above 99.9% confidence level), indicating that increase in strength of KWR corresponds to faster propagation of MJO. Note that the relation between the Kelvin wave index and MJO phase speed is not sensitive to the choice of zonal scale for calculating the Kelvin wave index.

It is noted that the Rossby wave responses can also be distilled by Hough function expansion, shown in Figs. 2e

and 2f. It shows that there are no significant differences of Rossby wave responses to the west of the MJO convection between the slow and fast MJO. However, there are Rossby wave anticyclones to the east of the MJO convection, which show some differences between the two MJO groups. These Rossby wave anticyclones are partially attributed to the dry anomalies over the WP (Kim et al. 2014) and partially attributed to the interaction between Rossby wave and westerly jets (Monteiro et al. 2014), which is an MJO–extratropical connection and could possibly affect the MJO phase speed (Yadav and Straus 2017). In fact, these Rossby wave anticyclones were shown to play important roles in MJO eastward propagation by enhancing premoistening in MC and WP through meridional winds (Kim et al. 2014; Feng et al. 2015; DeMott et al. 2018). To test the role of these Rossby wave anticyclones in causing the MJO speed variability, we define a Rossby wave index according to the Rossby wave meridional winds:

$$\text{Rossby wave index} = \frac{1}{60^{\circ}} \int_{\text{lon}_c + 20^{\circ}}^{\text{lon}_c + 80^{\circ}} \left( \frac{1}{20^{\circ}} \int_{0^{\circ}}^{20^{\circ}\text{N}} v_r d\text{lat} - \frac{1}{20^{\circ}} \int_{20^{\circ}\text{S}}^{0^{\circ}} v_r d\text{lat} \right) d\text{lon}, \quad (2)$$

where  $v_r$  is the meridional wind of the Rossby wave mode. Figure 3b shows that the Rossby wave index is weakly correlated to the MJO propagation speed with a correlation coefficient of 0.25, which is not significant at 95% level. Therefore, although the Rossby wave anticyclones to the east of the MJO convection contribute to the MJO eastward propagation, they are not the main cause of the MJO phase speed variability.



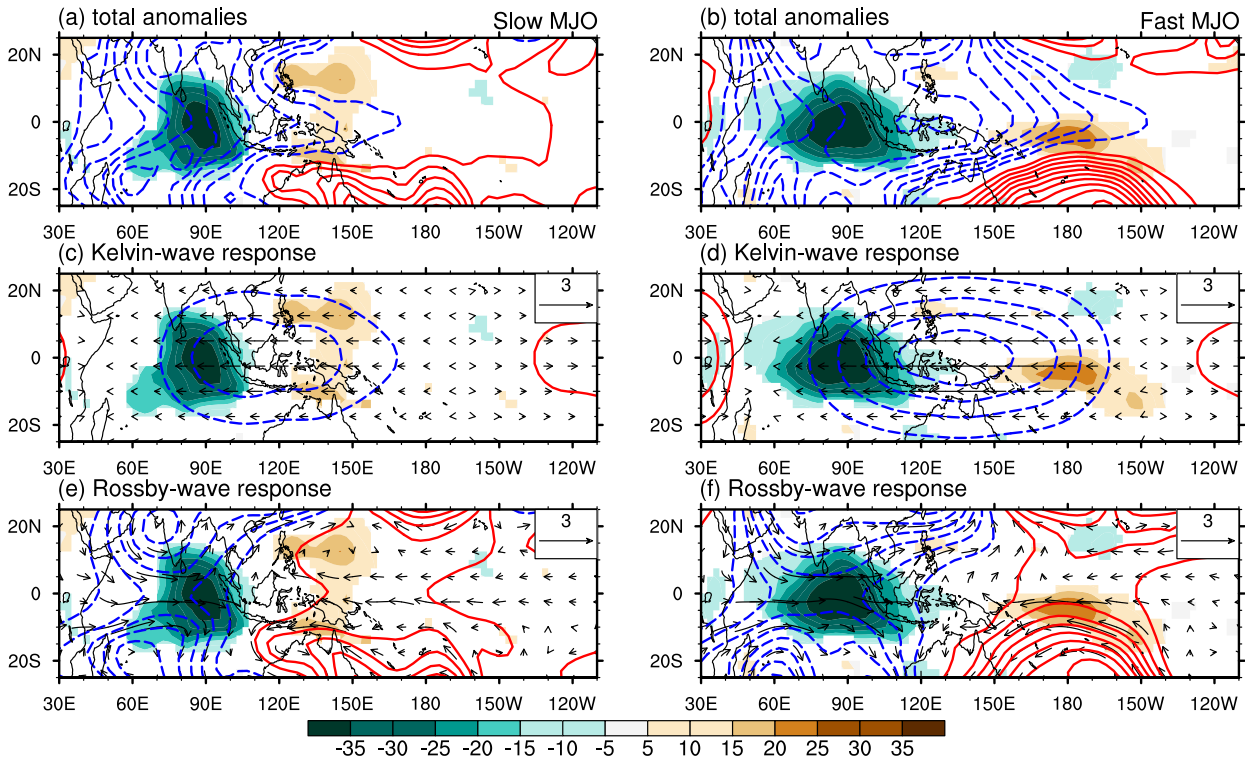


FIG. 2. Horizontal circulation features. The composited intraseasonal 850-hPa geopotential height anomalies (contours with interval of 2 m) and the OLR anomalies (shading in unit of  $\text{W m}^{-2}$ ) are shown for the (a) slow and (b) fast MJO events on peak phase of MJO convection in IO (pentad mean centered on day 0). For comparison, the variables have been scaled to a minimum equatorial ( $15^{\circ}\text{S}$ – $15^{\circ}\text{N}$  averaged) OLR of  $-30 \text{ W m}^{-2}$ . The stippled region indicates where the geopotential height anomalies are significant above 95% confidence level. The dashed contours indicate negative values, the solid contours indicate positive values, and the zero contours are omitted. (c),(d) The corresponding geopotential height anomalies (contours with interval of 2 m) and the wind anomalies (vectors;  $\text{m s}^{-1}$ ) contributed by the KWR, and (e),(f) the corresponding geopotential height anomalies (contours with interval of 2 m) and the wind anomalies contributed by the Rossby wave response. The corresponding OLR anomalies are also shown in (c)–(f). Only the OLR anomalies above 95% confidence level are shaded.

Since the zonal scale is another salient feature distinguishing the fast and slow MJO, we define a zonal scale index according to the zonal extent of the MJO convection. First, average the OLR from  $7.5^{\circ}\text{S}$  to  $7.5^{\circ}\text{N}$ . Second, scale the minimum OLR ( $7.5^{\circ}\text{S}$  to  $7.5^{\circ}\text{N}$  averaged) over  $45^{\circ}$ – $130^{\circ}\text{E}$  to  $-30 \text{ W m}^{-2}$  for each MJO event. Third, the zonal scale index is defined as number of grid point where OLR anomaly is below  $-3 \text{ W m}^{-2}$  from  $\text{lon}'_c - 40^{\circ}$  to  $\text{lon}'_c + 40^{\circ}$ , where  $\text{lon}'_c$  is the location of minimum OLR. Figure 3c shows that the zonal scale index is significantly correlated with the MJO phase speed with a correlation coefficient of 0.62, indicating that increase in MJO zonal scale corresponds to increase in the MJO phase speed.

As revealed by Figs. 1b and 1c, the fast MJO seems to have larger convection amplitude than the slow MJO. To check whether the MJO propagation speed is related to the MJO convection intensity, we define a mean MJO convection amplitude as  $A' = A/(T_2 - T_1)$ , where  $A$  is the accumulated amplitude along the tracking line (see appendix B) and  $T_1$  and  $T_2$  are the starting and ending

time of the tracking line. The correlation coefficient between  $A'$  and the MJO phase speed is about 0.07 (Fig. 3d), indicating that there is no significant correlation between the MJO convection amplitude and the MJO phase speed.

In summary, the variation of MJO propagation speed is significantly correlated with the intensity of the KWR and the zonal scale of the MJO. In next sections, we will show how the intensity of the KWR affects the MJO propagation speed and how the background mean states affect the KWR by changing the MJO zonal scale.

#### b. How the Kelvin wave response affects MJO propagation speed

Figures 4a and 4b compare the vertical thermal structures between the slow and fast MJO groups. In both the slow and fast propagating MJO groups, the low-level positive moisture anomalies (shadings) are found to lead (to the east of) the MJO deep convection, but the low-level premoistening is stronger and the moist layer is deeper in the fast group. Figure 4c further shows that the

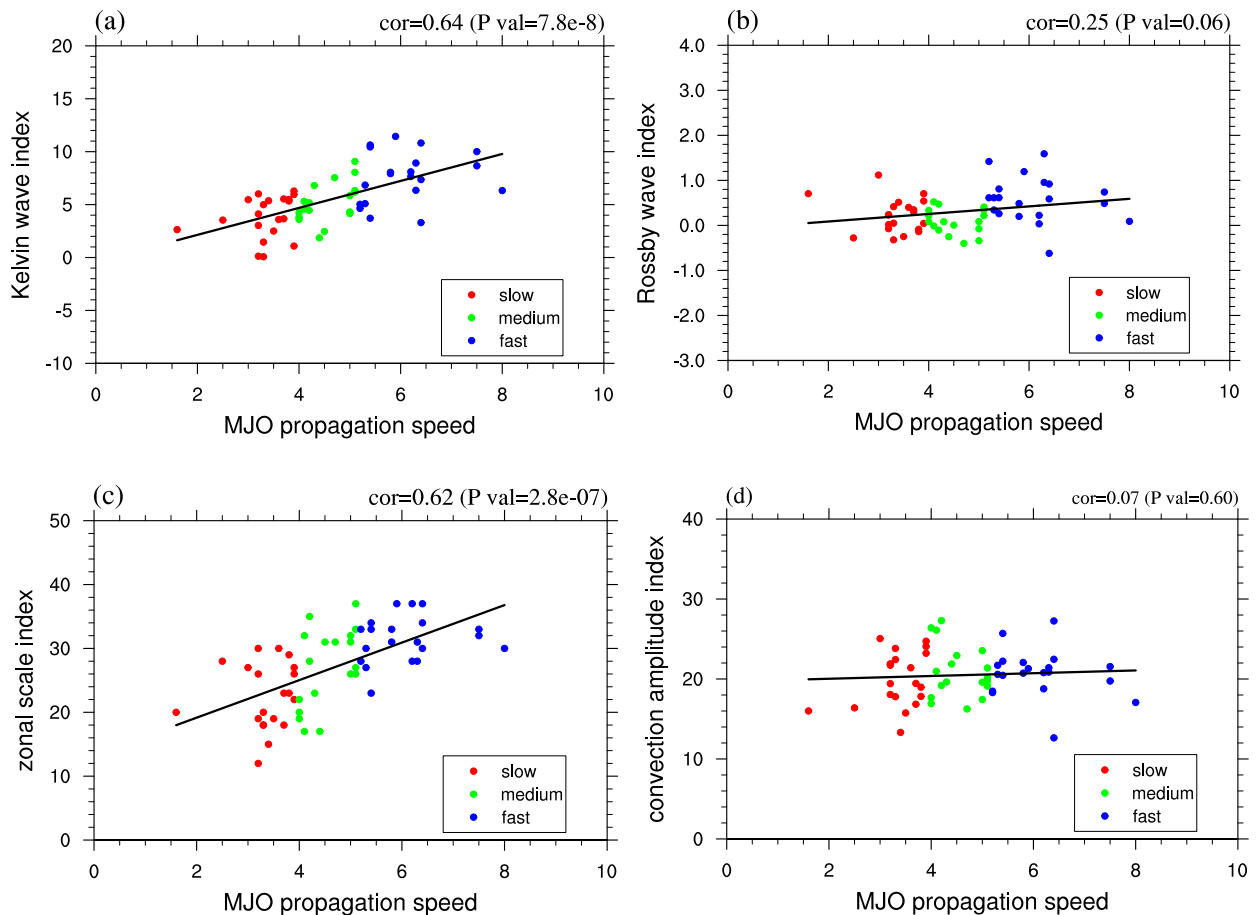


FIG. 3. The MJO propagation speed (in unit of  $\text{m s}^{-1}$ ) against the (a) Kelvin wave index (in unit of  $\text{m}$ ), (b) Rossby wave index (in unit of  $\text{m s}^{-1}$ ), (c) zonal scale index (number of grid point), and (d) convection amplitude index (in unit of  $\text{W m}^{-2}$ ). The linear correlation coefficients and the  $P$  values are shown. The red (blue) dots denote the slow (fast) MJO events, and the green dots denote the MJO events with propagation speed in between the fast and slow events.

leading low-level moisture anomalies are highly correlated with the strength of the KWR. This is because the low-level Kelvin wave low pressure can induce equatorial boundary layer (BL) convergence (Hendon and Salby 1994; Maloney and Hartmann 1998; Matthews 2000; Hsu and Li 2012; Wang and Lee 2017), leading to premoistening of the lower troposphere (Kiladis et al. 2005; Benedict and Randall 2007; Hsu and Li 2012; Chen and Wang 2018). Note that in slow MJO the moisture anomalies over MJO major convection zone ( $80^{\circ}$ – $100^{\circ}\text{E}$ ) are stronger than those in fast MJO. This is probably because the amplitude of the free atmospheric convergence is related to the zonal scale (as manifested by the term  $\partial u/\partial x$ ), with smaller zonal scale corresponding to stronger convergence. However, the BL convergence to the east of the MJO convection is forced by the low-level low pressure of KWR, which is dominant by meridional wind convergence (Wang and Li 1994) and is less sensitive to the zonal scale. In sum, a stronger KWR corresponds to

enhanced low-level premoistening to the east of MJO major convection.

The low-level premoistening can destabilize the lower to midtroposphere through increasing low-level moist static energy or equivalent potential temperature (Kemball-Cook and Weare 2001; Hsu and Li 2012; Wang and Lee 2017), paving the way for the development of shallow and congestus convection (Benedict and Randall 2007; Hsu and Li 2012). Figures 4a and 4b also exhibit the moisture sinks ( $Q_2$ ; contour) (Yanai et al. 1973), which, to some extent, represents the condensational heating. As the shallow and congestus convection have heating peaks below 700 hPa and pure deep convection can have heating peaks below 500 hPa (Shige et al. 2008; Takayabu et al. 2010), we interpret the lower tropospheric heating below 700 hPa as that associated with the shallow and congestus clouds. It shows that there is shallow and congestus convection developing in the region with low-level premoistening. The fast group

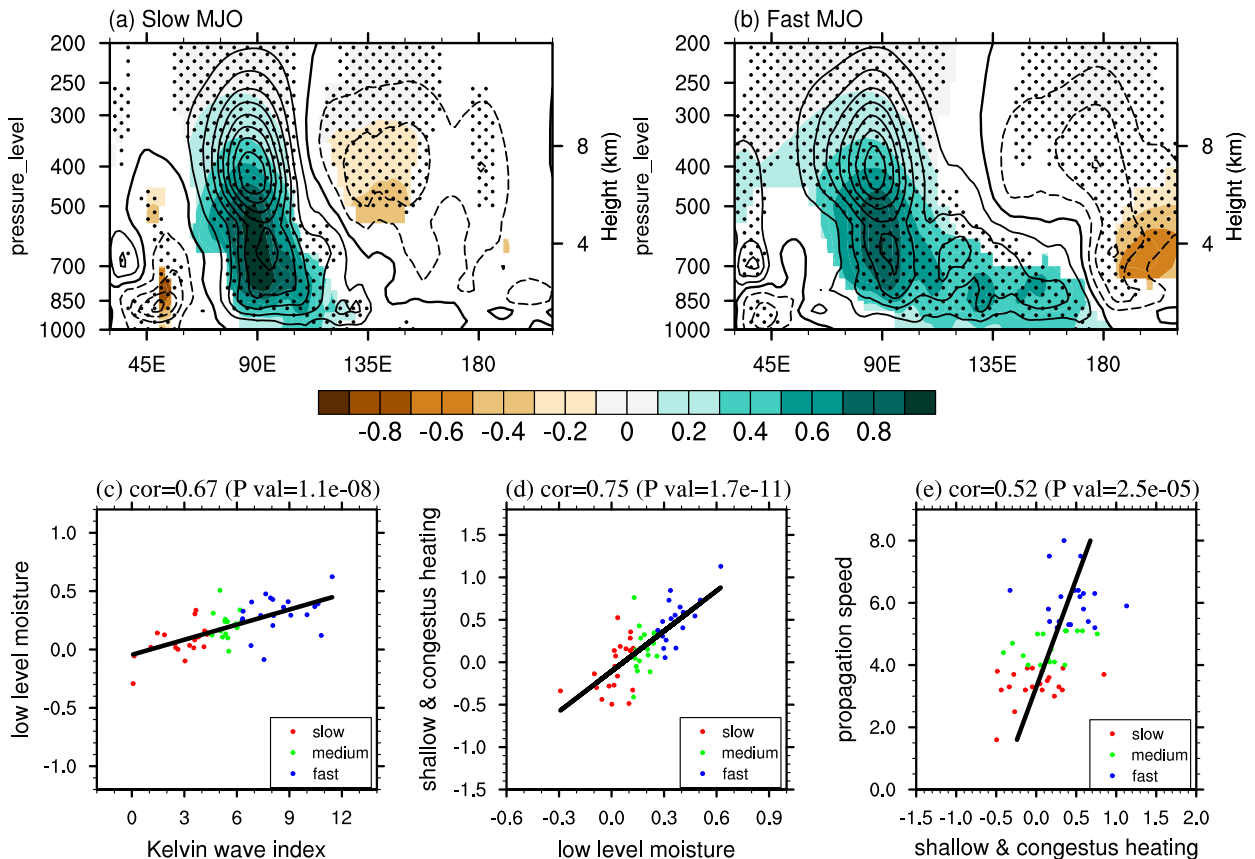


FIG. 4. Features of vertical structures. The composited vertical structures of the equatorial ( $10^{\circ}\text{S}$ – $10^{\circ}\text{N}$  averaged) specific humidity (shading in unit of  $\text{k kg}^{-1}$ ) and the moisture sinks (contours with interval of  $3 \times 10^{-3} \text{ J kg}^{-1} \text{ s}^{-1}$ ) are shown for the (a) slow and (b) fast groups on peak phase of MJO convection in the IO, respectively. The specific humidity anomalies are shown for those above 95% confidence level. The moisture sinks anomalies above the 95% confidence level are stippled. The dashed contours indicate negative values, the solid contours indicate positive values, and the thick solid contours denote zero contour. (c) The Kelvin wave index against the low-level moisture index, (d) the low-level moisture index against the shallow and congestus heating index, and (e) the shallow and congestus heating index against the MJO propagation speed. The low-level moisture index (in unit of  $\text{k kg}^{-1}$ ) is defined as vertically averaged (1000–750 hPa) specific humidity averaged between  $110^{\circ}\text{E}$  and  $180^{\circ}$ . The shallow and congestus heating index (in unit of  $10^{-2} \text{ J kg}^{-1} \text{ s}^{-1}$ ) is defined as vertically averaged (850–700 hPa) moisture sinks averaged between  $115^{\circ}$  and  $175^{\circ}\text{E}$ . For comparison, the variables in all panels (except the MJO speed) have been scaled to a minimum equatorial ( $15^{\circ}\text{S}$ – $15^{\circ}\text{N}$  averaged) OLR of  $-30 \text{ W m}^{-2}$ .

has stronger leading shallow and congestus convection than the slow group, as it has stronger low-level pre-moistening. Figure 4d supports that enhanced low-level moistening results in stronger shallow and congestus convection, as the low-level moisture is highly correlated with the shallow and congestus heating.

The well-developed congestus convection could further precondition the middle troposphere by eroding the dry midtroposphere, favoring the transition from congestus to deep convection (Johnson et al. 1999; Kikuchi and Takayabu 2004; Kuang and Bretherton 2006; Del Genio et al. 2012). It is manifest in Figs. 4a and 4b that the “developing stage” convection ( $105^{\circ}$ – $135^{\circ}\text{E}$ ), in which not only congestus but also sporadic deep convection are observed (Kikuchi and Takayabu 2004), is well established in the fast MJO. Thus, it

suggests that stronger congestus convection can lead to faster transition to deep convection, resulting in faster propagation of MJO deep convection. This is supported by the positive correlation between the MJO propagation speed and the shallow and congestus heating (Fig. 4e).

### c. The factors controlling the intensity of the Kelvin wave response

Theoretically, the MJO could be affected by the background BL and low-level moisture distribution (Wang et al. 2016; Wang and Chen 2017), and the background moisture content is determined by the background SST on monthly mean time scale (Wang 1988). Thus, it is conceivable that the variations in background SST states may cause variations in KWR

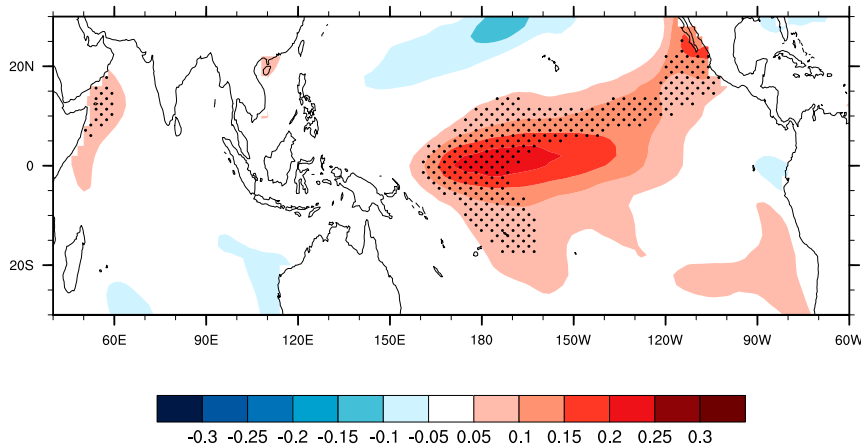


FIG. 5. Observed background SST variation with MJO speed. Shown are the background SST anomalies (in unit of  $\text{K m}^{-1} \text{s}$ ) regressed onto the MJO propagation speed. The stippled region indicates where the regressed background SST anomalies are significant at 95% confidence level. The background SST anomalies for an MJO event are defined as 3-month average of monthly SST anomalies (departure from climatological monthly mean), with the central month containing the day 0 of that MJO event.

and the MJO propagation speed. This is supported by Fig. 5 that an increase in MJO propagation speed is associated with equatorial central and eastern Pacific SST warming, reminiscent of an El Niño-like state.

How does the background SST variation over the central Pacific affect the KWR? The warming in the equatorial central Pacific leads to zonal expansion of the Indo-Pacific warm pool. Since the MJO activity is mainly observed over the warm ocean (Zhang 2005), an increase in zonal extent of the warm pool will lead to eastward expansion of MJO activity. Because the MJO tends to amplify on a longer zonal scale (Adames and Kim 2016; Fuchs and Raymond 2017; Chen and Wang 2019), the eastward expansion of MJO activity will result in increase of MJO zonal scale. This is manifested by the fact that the fast MJO has larger zonal scale (Figs. 2a,b). Using a theoretical model, Chen and Wang (2019) showed that the BL convergence feedback favors enhancing the KWR and this enhancing effect amplifies with increasing zonal scale of the MJO.

Thus, when the zonal scale of MJO expands, the KWR becomes stronger, explaining why the faster MJO has stronger KWR.

#### 4. Numerical results

To test this effect of warm-pool zonal scale on the MJO propagation speed, we conduct idealized experiments by using the theoretical model of Wang et al. (2016) and Wang and Chen (2017). The derivations of model equations are given in those works and here we elaborate the differences (the summarization of model formulations is given in appendix C). The major difference is that the precipitation is total field and is positive only in the original model (Wang and Chen 2017), while the precipitation is anomaly linearized about a climatological mean state in this study. This difference in precipitation definition does not affect the model formulations, assuming that the basic winds are weak and the effects of basic wind are negligible.

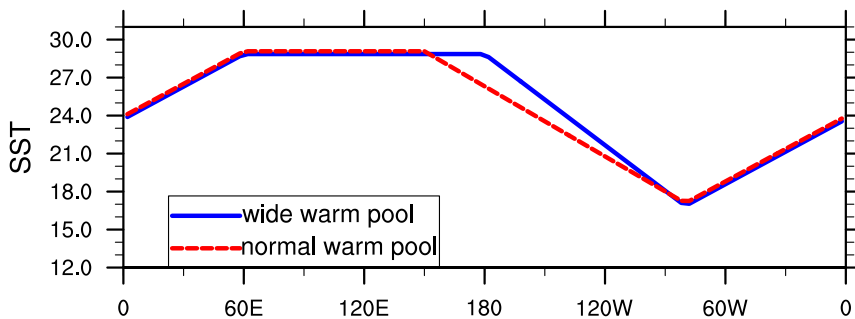


FIG. 6. Idealized SST ( $^{\circ}\text{C}$ ) distribution at the equator for the wide warm pool configuration (blue solid) and normal warm pool configuration (red dashed).



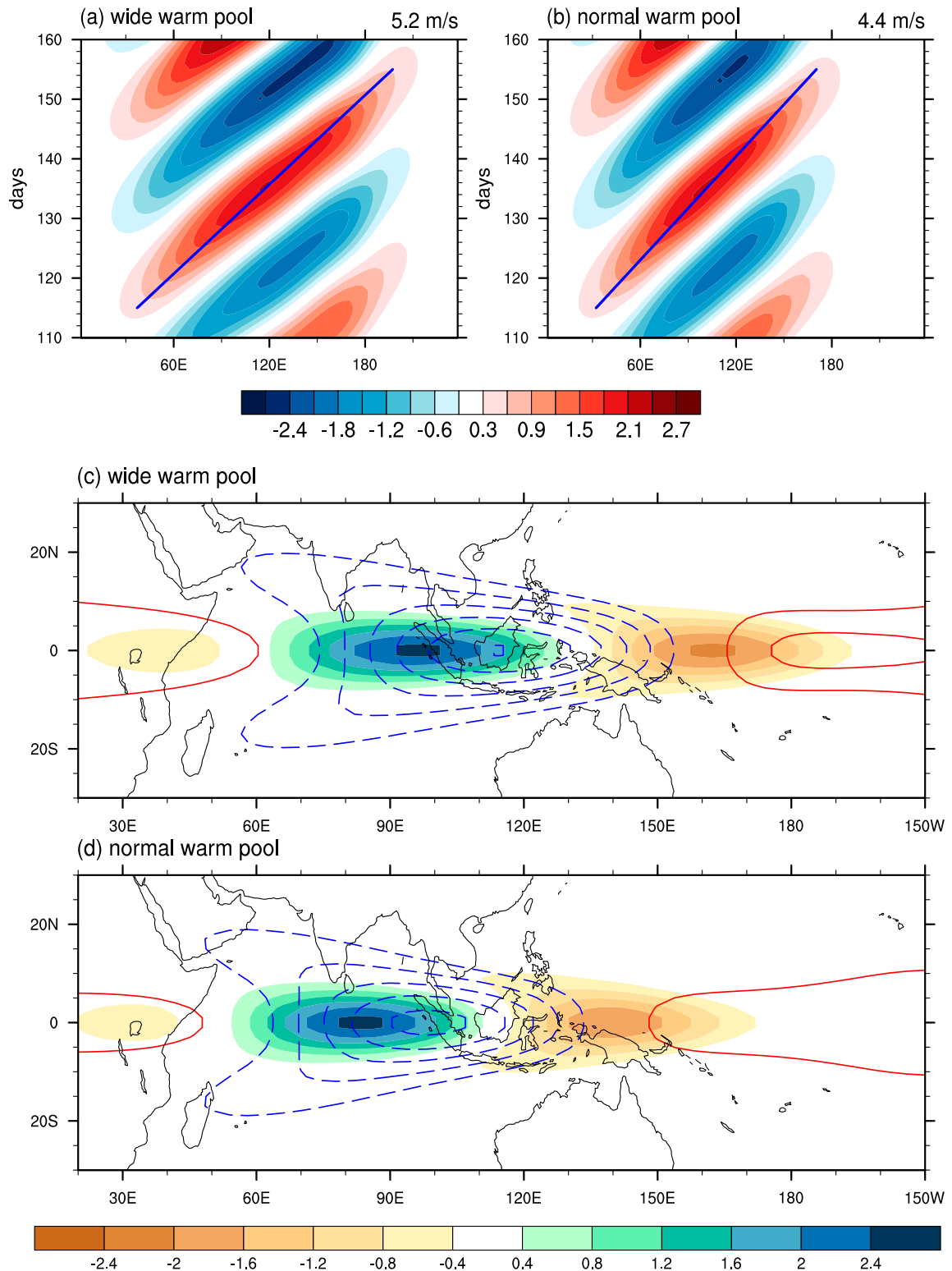


FIG. 7. Model test of the warm pool effect. The Hovmöller diagrams of the equatorial ( $5^{\circ}\text{S}$ – $5^{\circ}\text{N}$  averaged) precipitation anomalies (shading in unit of  $\text{mm day}^{-1}$ ) are shown for the (a) wide warm-pool simulation and (b) normal warm-pool simulation. (c),(d) The corresponding horizontal patterns of precipitation anomalies (shading in unit of  $\text{mm day}^{-1}$ ) and low-level geopotential height anomalies (contour with interval of 0.4 m) on day 130. The solid blue lines in (a) and (b) are least squares fits of the precipitation maximum.

The simplified Betts–Miller scheme (Frierson et al. 2004; Wang and Chen 2017) is used for precipitation parameterization:

$$\text{Pr} = \frac{(q + \alpha\phi)}{\tau}, \quad (3)$$

where Pr denotes precipitation anomaly,  $q$  is column moisture anomaly, and  $\phi$  is low-level geopotential anomaly;  $\alpha = 0.2$  is a nondimensional coefficient, and  $\tau$  is the convective time scale. According to Adames (2017),  $\tau$  for tropical precipitation anomaly is reversely related to the climatological mean precipitation. Therefore, we assume that  $\tau = \tau_0/\eta(\varphi)$ , where  $\tau_0 = 6\text{ h}$  and  $\eta(\varphi) = \exp[-(\varphi/10^\circ)^2]$ . Here,  $\varphi$  denotes latitude and  $\eta(\varphi)$  is the idealized meridional distribution of the climatological mean precipitation over the tropics.

In this model, the underlining background sea surface temperature controls the basic moisture states (Wang and Chen 2017). Here we assume that SST has a simple form of

$$\text{SST} = A(\lambda)B(\varphi), \quad (4)$$

where  $\lambda$  is longitude and  $B(\varphi) = \exp[-(\varphi/18^\circ)^2/4]$ .

To study the effect of the warm pool size, two idealized experiments will be conducted. One has a “normal” warm pool while the other has a “wide” warm pool. The function  $A(\lambda)$  associated with these two warm pool configurations are shown in Fig. 6. Note that the maximum warm pool SST in the normal warm pool setting is slightly higher than that in the wide warm pool setting (29.1°C vs 28.88°C). This difference is made so that the precipitation (convection) amplitudes in two simulations are comparable, because the MJO propagation speed can be reduced by strong convection as convection can reduce the effective stability felt by propagating waves (Bony and Emanuel 2005).

The results are shown in Fig. 7. It reveals that the precipitation anomalies in the wide warm pool simulation propagate faster than those in the normal warm pool simulation (Figs. 7a,b). Corresponding to faster eastward propagation, the zonal scales of the precipitation and circulation are larger and the associated KWR is stronger in the wide warm pool simulation (Figs. 7c,d). Thus, it is suggested that modifying Wang and Chen’s (2017) modeling could successfully represent the observational results that zonally expanded warm pool favors faster propagation of MJO through enlarging the MJO zonal scale and enhancing the KWR.

## 5. Conclusions and discussion

The factors controlling the propagation speed of the MJO are investigated. The results show that the observed

MJO propagation speed is related to the strength of the KWR, with a stronger KWR corresponding to faster MJO propagation. By amplifying low-level premoistening, a stronger KWR can enhance the zonal asymmetry in vertical thermal structures, as manifested by the enhanced leading shallow and congestus convection. The enhanced shallow and congestus convection preconditions the lower to midtroposphere, accelerating the transition to deep convection and leading to faster MJO propagation. The strength of the KWR is affected by the background SST variations in the central and eastern Pacific. For an El Niño–like state, the zonal scale of the Indo-Pacific warm pool expands. This leads to increase in the zonal scale of the MJO, which favors intensifying the KWR. This effect of warm pool zonal scale has been verified by using a theoretical model.

Previous theoretical and model studies have revealed that the MJO propagation speed is related to the relative strength between the Kelvin and Rossby wave response to the east and west of the MJO convection, measured by ratio between the Kelvin and Rossby wave responses (Kang et al. 2013; Wang and Chen 2017; Wang and Lee 2017; Chen and Wang 2019), with stronger Kelvin (Rossby) wave response corresponding to faster (slower) propagation speed. In this study, we show that the observed fast and slow MJO are only distinguished by the KWRs. In fact, this result supports the previous studies, only that the change of Kelvin–Rossby ratio is mainly manifested in the change of the KWR.

The results of this study have implications on the MJO prediction in two aspects. First, it suggests that when the MJO develops in the eastern IO region, the structures of the MJO can be considered as precursors for the MJO propagation speed: when the zonal scale of the MJO convectively coupled system is large and the associated KWR is strong, it is highly possible that the MJO will propagate eastward faster, and vice versa. Second, it also suggests that the background SST variation in the equatorial central Pacific is another precursor for foreseeing the MJO propagation: when the equatorial central Pacific warms, it is expected that the MJO propagation will speed up and the fast propagating MJO events will occur more frequently.

*Acknowledgments.* This work is jointly supported by the National Key R&D Program of China (Grant 2018YFC1505905), the National Natural Science Foundation of China (Grant 2081011900501), the NSF/Climate Dynamics Award AGS-1540783, and the NOAA/CVP Award NA15OAR4310177. This is the SEOST publication 10918, IPRC publication 1433, and ESMC publication 301.

## APPENDIX A

## Hough Function Expansion

According to [Kasahara \(1976\)](#) and [Kasahara and Puri \(1981\)](#), single-level atmospheric data  $\mathbf{X}(\lambda, \varphi) = (u, v, h)^T$  can be projected to Hough harmonics as

$$\mathbf{S}^{-1}\mathbf{X} = \sum_{l=1}^L \sum_{k=-M}^M X_l^k \mathbf{H}_l^k(\lambda, \varphi), \quad (\text{A1})$$

where  $\lambda$  and  $\varphi$  denote longitude and latitude respectively;  $u$ ,  $v$ , and  $h$  are zonal wind, meridional wind, and geopotential height, respectively; and  $\mathbf{S}$  is a  $3 \times 3$  diagonal matrix with diagonal elements  $\sqrt{gD_0}$ ,  $\sqrt{gD_0}$ , and  $D_0$ , where  $D_0$  is the equivalent geopotential height determined by the vertical structural equation of the atmosphere. In this study, we chose  $D_0 = 250$  m. This is because the baroclinic vertical structure of the tropical tropospheric circulation associated with the MJO is similar to that prescribed by the vertical structure function with  $D_0 \approx 250$  m ([Kasahara and Puri 1981](#)).

$\mathbf{H}_l^k(\lambda, \varphi)$  is the Hough function, where  $l$  and  $k$  represent meridional mode and zonal wavenumber respectively. In this study, we chose  $k = \pm 1, \pm 2, \dots, \pm 16$ . The scalar coefficient  $X_l^k$  can be obtained as

$$X_l^k = \frac{1}{2\pi} \int_0^{2\pi} \int_{-1}^1 \mathbf{S}^{-1}\mathbf{X}[\mathbf{H}_l^k(\lambda, \varphi)]^* d\mu d\lambda, \quad (\text{A2})$$

where  $\mu = \sin\varphi$  and the asterisk denotes complex conjugate.

By choosing certain  $l$ , the atmospheric data can be projected onto certain wave mode. For example, the Kelvin wave mode (the first mode in the eastward gravity wave modes) can be obtained as

$$\mathbf{S}^{-1}\mathbf{X}^{l_K} = \sum_{k=-M}^M X_{l_K}^k \mathbf{H}_{l_K}^k(\lambda, \varphi), \quad (\text{A3})$$

where  $l_K$  denotes Kelvin wave mode.

## APPENDIX B

## MJO Tracking Method

The method for MJO tracking in this study is a modified version of the one proposed by [Zhang and Ling \(2017\)](#). The essence of this method is to find a tracking line that best describes the eastward propagation of the MJO convection anomalies in the time–longitude section. This is done by the following steps:

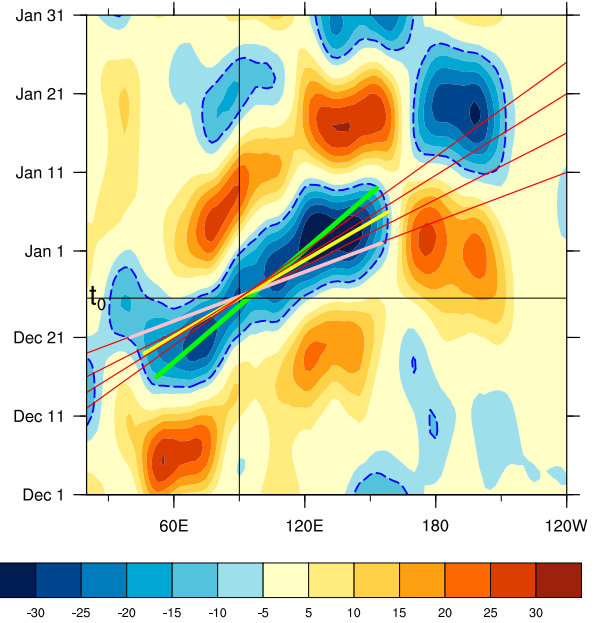


FIG. B1. Example of the MJO tracking. The shading denotes the OLR anomalies ( $10^{\circ}\text{S}$ – $10^{\circ}\text{N}$  averaged) from December 2006 to January 2007. The dashed contours outline the  $-10 \text{ W m}^{-2}$  OLR. The thin red lines are examples of trial lines passing through reference longitude at day  $t_0$ . The pink line is an example of candidate tracking line. The green line is the final tracking line for the given MJO event. The yellow line is the final tracking line obtained by the original method of [Zhang and Ling \(2017\)](#).

- (i) Plot Hovmöller (time–longitude) diagram of the intraseasonal equatorial OLR anomalies ( $10^{\circ}\text{S}$ – $10^{\circ}\text{N}$  averaged) for each winter season. Apply a zonal 5-point running mean to the Hovmöller diagram.
- (ii) Select a reference longitude and a tracking domain. In this study,  $90^{\circ}\text{E}$  is chosen as the reference longitude, as done by [Zhang and Ling \(2017\)](#). The tracking domain is defined as  $20^{\circ}\text{E}$ – $140^{\circ}\text{W}$ . This choice of tracking domain and reference longitude facilitates tracking of those selected MJO events.
- (iii) Denote day 0 of a selected MJO event as  $t_0$ . At a given day  $t \in [t_0 - 12 \text{ days}, t_0 + 12 \text{ days}]$ , run a set of trial lines passing the reference longitude with different slopes, as shown in [Fig. B1](#) (solid red lines). The slope of a tracking line represents the speed of zonal propagation. In this study, the slopes (or speed  $c$ ) are ranging from  $1$  to  $25 \text{ m s}^{-1}$  with intervals of  $0.1 \text{ m s}^{-1}$ . Use coordinate  $(t, c)$  to represent the trial line that passes the reference longitude at day  $t$  with speed  $c$ .
- (iv) Identify segments along a trial line that satisfied  $\text{OLR} < -10 \text{ W m}^{-2}$  (e.g., the segments that are within the blue dashed contour shown in [Fig. B1](#)). Treat two segments as one if the longitude gap between them is smaller than  $10^{\circ}$ .

- (v) Select the longest segment on a trial line. The thick pink line in Fig. B1 is an example of the longest segment on a trial line. The longest segment in a trial line is a candidate tracking line for an MJO event.
- (vi) Compute the accumulated amplitude  $A(t, c)$  and longitude span  $L(t, c)$  of a candidate tracking line. The accumulated amplitude  $A(t, c)$  is the sum of OLR values over the grid points along a candidate tracking line, and the longitude span  $L(t, c)$  is the difference between the ending and starting longitudes of a candidate tracking line. Note that in Zhang and Ling (2017),  $A(t, c)$  is the integrated OLR along a candidate tracking line.
- (vii) Repeat steps (iii) to (vi) for  $t \in [t_0 - 12 \text{ days}, t_0 + 12 \text{ days}]$ . As a result, the accumulated amplitude  $A(t, c)$  and longitude span  $L(t, c)$  of a given MJO event are obtained.
- (viii) Define a function  $B(t, c) = A(t, c)/A_m(t, c) + L(t, c)/L_m(t, c)$  for an MJO event, where  $A_m(t, c)$  and  $L_m(t, c)$  are the maximum accumulated amplitude and longitude span over the domain of  $[t_0 - 12: t_0 + 12, 1: 25 \text{ m s}^{-1}]$ . Find maximum  $B(t, c)$  [denoted as  $B_m(t, c)$ ]. The candidate tracking line corresponding to  $B_m(t, c)$  is chosen as the final tracking line for an MJO event (e.g., the thick green line in Fig. B1).

The major differences between this modified tracking method and the original one (Zhang and Ling 2017) are that the tracking line is defined as the one having  $B_m(t, v)$  instead of  $A_m(t, v)$  and the definition of  $A(t, c)$  is different. The yellow line is the final tracking line obtained by the original method of Zhang and Ling (2017). It shows that the original method tends to overestimate the propagation speed. Overall, in some cases the two methods have similar results, while in other cases the original one tends to overestimate the propagation speed. It should be noted that both methods may contain some uncertainties.

## APPENDIX C

### Theoretical Model

The nondimensional governing equations are as follows:

$$\left(\frac{\partial}{\partial t} + \mu\right)u - yv = -\frac{\partial\Phi}{\partial x}, \quad (\text{C1})$$

$$\left(\frac{\partial}{\partial t} + \mu\right)v + yu = -\frac{\partial\Phi}{\partial y}, \quad (\text{C2})$$

$$\left(\frac{\partial}{\partial t} + \mu\right)\Phi + D + dD_b = -\text{Pr} - R, \quad (\text{C3})$$

$$\frac{\partial q}{\partial t} + \overline{Q}D + d\overline{Q}_b D_b + \mathbf{V} \cdot \nabla \overline{Q} + d\mathbf{V}_b \cdot \nabla \overline{Q}'_b = Ev - \text{Pr}, \quad (\text{C4})$$

$$\frac{\partial u_b}{\partial t} - yv_b = -\frac{\partial\Phi}{\partial x} - Eu_b, \quad (\text{C5})$$

$$\frac{\partial v_b}{\partial t} + yu_b = -\frac{\partial\Phi}{\partial y} - Ev_b. \quad (\text{C6})$$

Equations (C1) and (C2) are momentum equations. Equation (C3) is the combined hydrostatic, continuity, and thermodynamic equation. Equation (C4) is the vertically integrated moisture equation. Equations (C5) and (C6) are momentum equations for a barotropic BL. The terms  $u$ ,  $v$ , and  $\Phi$  represent the free-tropospheric low-level zonal wind, meridional wind, and geopotential anomalies;  $\mathbf{V}$  and  $\mathbf{V}_b$  denote the wind vector anomalies at the low-level free atmosphere and the BL;  $\mu$  denotes the damping rate, which is set to  $1/(12 \text{ days})$ ;  $q$  is the column-integrated perturbation moisture from the top of the BL to the tropopause;  $\text{Pr}$ ,  $R$ , and  $Ev$  are precipitation rate, longwave radiation, and evaporation anomalies. In this study,  $Ev$  is neglected and  $R = \varepsilon \text{Pr}$ , with  $\varepsilon = 0.16$ . Also,  $\overline{Q}$  denotes the difference of normalized basic-state specific humidity between the lower and upper layer,  $\overline{Q}_b$  denotes the difference of normalized basic-state specific humidity between the BL and the upper layer, and  $\overline{Q}'_b$  denotes the normalized basic-state specific humidity at BL;  $\overline{Q}$ ,  $\overline{Q}_b$ , and  $\overline{Q}'_b$  are controlled by the underlying SST (Wang and Chen 2017). The terms  $D$  and  $D_b$  are the lower-tropospheric and BL divergence, respectively;  $u_b$  and  $v_b$  are BL barotropic winds,  $E = 1/(0.5 \text{ day})$  is the friction coefficient in the BL, and ( $d = 1/4$ ) is the nondimensional BL depth. For more details, the readers are referred to Wang et al. (2016), Wang and Chen (2017), and Chen and Wang (2019).

## REFERENCES

- Adames, Á. F., 2017: Precipitation budget of the Madden-Julian oscillation. *J. Atmos. Sci.*, **74**, 1799–1817, <https://doi.org/10.1175/JAS-D-16-0242.1>.
- , and D. Kim, 2016: The MJO as a dispersive, convectively coupled moisture wave: Theory and observations. *J. Atmos. Sci.*, **73**, 913–941, <https://doi.org/10.1175/JAS-D-15-0170.1>.
- Benedict, J. J., and D. A. Randall, 2007: Observed characteristics of the MJO relative to maximum rainfall. *J. Atmos. Sci.*, **64**, 2332–2354, <https://doi.org/10.1175/JAS3968.1>.
- Bony, S., and K. A. Emanuel, 2005: On the role of moist processes in tropical intraseasonal variability: Cloud–radiation and moisture–convection feedbacks. *J. Atmos. Sci.*, **62**, 2770–2789, <https://doi.org/10.1175/JAS3506.1>.
- Chen, G., and B. Wang, 2018: Effects of enhanced front Walker cell on the eastward propagation of the MJO. *J. Climate*, **31**, 7719–7738, <https://doi.org/10.1175/JCLI-D-17-0383.1>.

- , and —, 2019: Dynamic moisture mode versus moisture mode in MJO dynamics: Importance of the wave feedback and boundary layer convergence feedback. *Climate Dyn.*, **52**, 5127–5143, <https://doi.org/10.1007/s00382-018-4433-7>.
- Dee, D. P., and Coauthors, 2011: The ERA-Interim reanalysis: Configuration and performance of the data assimilation system. *Quart. J. Roy. Meteor. Soc.*, **137**, 553–597, <https://doi.org/10.1002/qj.828>.
- Del Genio, A. D., Y. Chen, D. Kim, and M.-S. Yao, 2012: The MJO transition from shallow to deep convection in *CloudSat*/CALIPSO data and GISS GCM simulations. *J. Climate*, **25**, 3755–3770, <https://doi.org/10.1175/JCLI-D-11-00384.1>.
- DeMott, C. A., B. O. Wolding, E. D. Maloney, and D. A. Randall, 2018: Atmospheric mechanisms for MJO decay over the Maritime Continent. *J. Geophys. Res. Atmos.*, **123**, 5188–5204, <https://doi.org/10.1029/2017JD026979>.
- Duchon, C. E., 1979: Lanczos filtering in one and two dimensions. *J. Appl. Meteor.*, **18**, 1016–1022, [https://doi.org/10.1175/1520-0450\(1979\)018<1016:LFFIOAT>2.0.CO;2](https://doi.org/10.1175/1520-0450(1979)018<1016:LFFIOAT>2.0.CO;2).
- Feng, J., T. Li, and W. Zhu, 2015: Propagating and nonpropagating MJO events over Maritime Continent. *J. Climate*, **28**, 8430–8449, <https://doi.org/10.1175/JCLI-D-15-0085.1>.
- Frierson, D. M., A. J. Majda, and O. M. Pauluis, 2004: Large scale dynamics of precipitation fronts in the tropical atmosphere: A novel relaxation limit. *Commun. Math. Sci.*, **2**, 591–626, <https://doi.org/10.4310/CMS.2004.v2.n4.a3>.
- Fuchs, Z., and D. J. Raymond, 2017: A simple model of intraseasonal oscillations. *J. Adv. Model. Earth Syst.*, **9**, 1195–1211, <https://doi.org/10.1002/2017MS000963>.
- Gill, A. E., 1980: Some simple solutions for heat-induced tropical circulation. *Quart. J. Roy. Meteor. Soc.*, **106**, 447–462, <https://doi.org/10.1002/qj.49710644905>.
- Hendon, H. H., and M. L. Salby, 1994: The life cycle of the Madden–Julian Oscillation. *J. Atmos. Sci.*, **51**, 2225–2237, [https://doi.org/10.1175/1520-0469\(1994\)051<2225:TLCOTM>2.0.CO;2](https://doi.org/10.1175/1520-0469(1994)051<2225:TLCOTM>2.0.CO;2).
- Hsu, P., and T. Li, 2012: Role of the boundary layer moisture asymmetry in causing the eastward propagation of the Madden–Julian oscillation. *J. Climate*, **25**, 4914–4931, <https://doi.org/10.1175/JCLI-D-11-00310.1>.
- Huang, B., and Coauthors, 2017: Extended Reconstructed Sea Surface Temperature, version 5 (ERSSTv5): Upgrades, validations, and intercomparisons. *J. Climate*, **30**, 8179–8205, <https://doi.org/10.1175/JCLI-D-16-0836.1>.
- Jiang, X., 2017: Key processes for the eastward propagation of the Madden–Julian Oscillation based on multimodel simulations. *J. Geophys. Res. Atmos.*, **122**, 755–770, <https://doi.org/10.1002/2016JD025955>.
- , and Coauthors, 2015: Vertical structure and physical processes of the Madden–Julian oscillation: Exploring key model physics in climate simulations. *J. Geophys. Res. Atmos.*, **120**, 4718–4748, <https://doi.org/10.1002/2014JD022375>.
- , Á. F. Adames, M. Zhao, D. Waliser, and E. Maloney, 2018: A unified moisture mode framework for seasonality of the Madden–Julian oscillation. *J. Climate*, **31**, 4215–4224, <https://doi.org/10.1175/JCLI-D-17-0671.1>.
- Johnson, R. H., T. M. Rickenbach, S. A. Rutledge, P. E. Ciesielski, and W. H. Schubert, 1999: Trimodal characteristics of tropical convection. *J. Climate*, **12**, 2397–2418, [https://doi.org/10.1175/1520-0442\(1999\)012<2397:TCOTC>2.0.CO;2](https://doi.org/10.1175/1520-0442(1999)012<2397:TCOTC>2.0.CO;2).
- Kang, I.-S., F. Liu, M.-S. Ahn, Y.-M. Yang, and B. Wang, 2013: The role of SST structure in convectively coupled Kelvin–Rossby waves and its implications for MJO formation. *J. Climate*, **26**, 5915–5930, <https://doi.org/10.1175/JCLI-D-12-00303.1>.
- Kasahara, A., 1976: Normal modes of ultralong waves in the atmosphere. *Mon. Wea. Rev.*, **104**, 669–690, [https://doi.org/10.1175/1520-0493\(1976\)104<0669:NMOUWI>2.0.CO;2](https://doi.org/10.1175/1520-0493(1976)104<0669:NMOUWI>2.0.CO;2).
- , and K. Puri, 1981: Spectral representation of three-dimensional global data by expansion in normal mode functions. *Mon. Wea. Rev.*, **109**, 37–51, [https://doi.org/10.1175/1520-0493\(1981\)109<0037:SROTDG>2.0.CO;2](https://doi.org/10.1175/1520-0493(1981)109<0037:SROTDG>2.0.CO;2).
- Kemball-Cook, S. R., and B. C. Weare, 2001: The onset of convection in the Madden–Julian oscillation. *J. Climate*, **14**, 780–793, [https://doi.org/10.1175/1520-0442\(2001\)014<0780:TOOCIT>2.0.CO;2](https://doi.org/10.1175/1520-0442(2001)014<0780:TOOCIT>2.0.CO;2).
- Kikuchi, K., and Y. N. Takayabu, 2004: The development of organized convection associated with the MJO during TOGA COARE IOP: Trimodal characteristics. *Geophys. Res. Lett.*, **31**, L10101, <https://doi.org/10.1029/2004GL019601>.
- , B. Wang, and Y. Kajikawa, 2012: Bimodal representation of the tropical intraseasonal oscillation. *Climate Dyn.*, **38**, 1989–2000, <https://doi.org/10.1007/s00382-011-1159-1>.
- Kiladis, G. N., K. H. Straub, and P. T. Haertel, 2005: Zonal and vertical structure of the Madden–Julian oscillation. *J. Atmos. Sci.*, **62**, 2790–2809, <https://doi.org/10.1175/JAS3520.1>.
- Kim, D., J.-S. Kug, and A. H. Sobel, 2014: Propagating versus nonpropagating Madden–Julian oscillation events. *J. Climate*, **27**, 111–125, <https://doi.org/10.1175/JCLI-D-13-00084.1>.
- Knutson, T. R., K. M. Weickmann, and J. E. Kutzbach, 1986: Global-scale intraseasonal oscillations of outgoing longwave radiation and 250 mb zonal wind during Northern Hemisphere summer. *Mon. Wea. Rev.*, **114**, 605–623, [https://doi.org/10.1175/1520-0493\(1986\)114<0605:GSI000>2.0.CO;2](https://doi.org/10.1175/1520-0493(1986)114<0605:GSI000>2.0.CO;2).
- Kuang, Z., and C. S. Bretherton, 2006: A mass-flux scheme view of a high-resolution simulation of a transition from shallow to deep cumulus convection. *J. Atmos. Sci.*, **63**, 1895–1909, <https://doi.org/10.1175/JAS3723.1>.
- Liebmann, B., and C. Smith, 1996: Description of a complete (interpolated) outgoing longwave radiation dataset. *Bull. Amer. Meteor. Soc.*, **77**, 1275–1277.
- Longuet-Higgins, M. S., 1968: The eigenfunctions of Laplace’s tidal equation over a sphere. *Philos. Trans. Roy. Soc. London*, **A262**, 511–607, <https://doi.org/10.1098/rsta.1968.0003>.
- Madden, R. A., and P. R. Julian, 1972: Description of global-scale circulation cells in the tropics with a 40–50 day period. *J. Atmos. Sci.*, **29**, 1109–1123, [https://doi.org/10.1175/1520-0469\(1972\)029<1109:DOGSCC>2.0.CO;2](https://doi.org/10.1175/1520-0469(1972)029<1109:DOGSCC>2.0.CO;2).
- Maloney, E. D., and D. L. Hartmann, 1998: Frictional moisture convergence in a composite life cycle of the Madden–Julian oscillation. *J. Climate*, **11**, 2387–2403, [https://doi.org/10.1175/1520-0442\(1998\)011<2387:FMCIAC>2.0.CO;2](https://doi.org/10.1175/1520-0442(1998)011<2387:FMCIAC>2.0.CO;2).
- Matsuno, T., 1966: Quasi-geostrophic motions in the equatorial area. *J. Meteor. Soc. Japan*, **44**, 25–43, [https://doi.org/10.2151/jmsj1965.44.1\\_25](https://doi.org/10.2151/jmsj1965.44.1_25).
- Matthews, A. J., 2000: Propagation mechanisms for the Madden–Julian Oscillation. *Quart. J. Roy. Meteor. Soc.*, **126**, 2637–2651, <https://doi.org/10.1002/qj.49712656902>.
- Monteiro, J. M., Á. F. Adames, J. M. Wallace, and J. S. Sukhatme, 2014: Interpreting the upper level structure of the Madden–Julian Oscillation. *Geophys. Res. Lett.*, **41**, 9158–9165, <https://doi.org/10.1002/2014GL062518>.
- Shige, S., Y. N. Takayabu, and W.-K. Tao, 2008: Spectral retrieval of latent heating profiles from TRMM PR data. Part III: Estimating apparent moisture sink profiles over tropical oceans. *J. Appl. Meteor. Climatol.*, **47**, 620–640, <https://doi.org/10.1175/2007JAMC1738.1>.



- Takayabu, Y. N., S. Shige, W.-K. Tao, and N. Hirota, 2010: Shallow and deep latent heating modes over tropical oceans observed with TRMM PR spectral latent heating data. *J. Climate*, **23**, 2030–2046, <https://doi.org/10.1175/2009JCLI3110.1>.
- Wang, B., 1988: Dynamics of tropical low-frequency waves: An analysis of the moist Kelvin wave. *J. Atmos. Sci.*, **45**, 2051–2065, [https://doi.org/10.1175/1520-0469\(1988\)045<2051:DOTLFW>2.0.CO;2](https://doi.org/10.1175/1520-0469(1988)045<2051:DOTLFW>2.0.CO;2).
- , and T. Li, 1994: Convective interaction with boundary-layer dynamics in the development of a tropical intraseasonal system. *J. Atmos. Sci.*, **51**, 1386–1400, [https://doi.org/10.1175/1520-0469\(1994\)051<1386:CIWBLD>2.0.CO;2](https://doi.org/10.1175/1520-0469(1994)051<1386:CIWBLD>2.0.CO;2).
- , and X. Xie, 1997: A model for the boreal summer intraseasonal oscillation. *J. Atmos. Sci.*, **54**, 72–86, [https://doi.org/10.1175/1520-0469\(1997\)054<0072:AMFTBS>2.0.CO;2](https://doi.org/10.1175/1520-0469(1997)054<0072:AMFTBS>2.0.CO;2).
- , and G. Chen, 2017: A general theoretical framework for understanding essential dynamics of Madden–Julian oscillation. *Climate Dyn.*, **49**, 2309–2328, <https://doi.org/10.1007/s00382-016-3448-1>.
- , and S.-S. Lee, 2017: MJO propagation shaped by zonal asymmetric structures: Results from 24 GCM simulations. *J. Climate*, **30**, 7933–7952, <https://doi.org/10.1175/JCLI-D-16-0873.1>.
- , F. Liu, and G. Chen, 2016: A trio-interaction theory for Madden–Julian Oscillation. *Geosci. Lett.*, **3**, 34, <https://doi.org/10.1186/s40562-016-0066-z>.
- , and Coauthors, 2018: Dynamics-oriented diagnostics for the Madden–Julian oscillation. *J. Climate*, **31**, 3117–3135, <https://doi.org/10.1175/JCLI-D-17-0332.1>.
- , G. Chen, and F. Liu, 2019: Diversity of the Madden–Julian Oscillation. *Sci. Adv.*, **5**, eaax0220, <https://doi.org/10.1126/sciadv.aax0220>.
- Yadav, P., and D. M. Straus, 2017: Circulation response to fast and slow MJO episodes. *Mon. Wea. Rev.*, **145**, 1577–1596, <https://doi.org/10.1175/MWR-D-16-0352.1>.
- Yanai, M., S. Esbensen, and J.-H. Chu, 1973: Determination of bulk properties of tropical cloud clusters from large-scale heat and moisture budgets. *J. Atmos. Sci.*, **30**, 611–627, [https://doi.org/10.1175/1520-0469\(1973\)030<0611:DOBPOT>2.0.CO;2](https://doi.org/10.1175/1520-0469(1973)030<0611:DOBPOT>2.0.CO;2).
- Žagar, N., and C. L. E. Franzke, 2015: Systematic decomposition of the Madden–Julian Oscillation into balanced and inertio-gravity components. *Geophys. Res. Lett.*, **42**, 6829–6835, <https://doi.org/10.1002/2015GL065130>.
- Zhang, C., 2005: Madden–Julian Oscillation. *Rev. Geophys.*, **43**, RG2003, <https://doi.org/10.1029/2004RG000158>.
- , and J. Ling, 2017: Barrier effect of the Indo-Pacific Maritime Continent on the MJO: Perspectives from tracking MJO precipitation. *J. Climate*, **30**, 3439–3459, <https://doi.org/10.1175/JCLI-D-16-0614.1>.